Reconstructing 3-D FRI shapes from tomographic projections at unknown angles

Kate L.Y. Zhao, Renke Wang, Pier Luigi Dragotti
Dept. of Electrical and Electronic Engineering, Imperial College London
{kate.zhao22, renke.wang19, p.dragotti}@imperial.ac.uk

***Abstract*—Conventional methods for 3-D reconstruction from 2-D tomographic projections require prior knowledge of projection orientation. Without such information, reconstruction typically becomes a non-convex optimization problem. However, previous work has demonstrated perfect reconstruction of bilevel convex polyhedra from unknown orientations given a minimum number of projections. In this paper, we further extend that theory by generalizing reconstruction to arbitrary shapes. We represent objects and their projections as multidimensional finite rate of innovation (FRI) signals. We retrieve FRI parameters through the use of isotropic, exponential approximating kernels to obtain the signal's exponential moments, followed by application of 2-D harmonic retrieval methods. FRI parameters are then paired across different projections. Finally, an algebraic method is applied to retrieve the orientation angles of the samples, allowing for successful reconstruction.**

***Index Terms*—multidimensional sampling, exponential approximation, cryogenic electron microscopy (cryo-EM), finite rate of innovation (FRI), 3-D reconstruction, sampling at unknown locations, unknown view tomography (UVT)**

I. Introduction

The technology to reconstruct 3-D volumes from their 2-D projections has revolutionized numerous imaging applications across several fields. These include macroscopic tasks in vision-based domains, such as object recognition and motion capture [1], or in medical imaging, for example in CT scanning and diagnostics [2]. With improvements in capture and processing technology over the past decades, biological structures that comprise the fundamental building blocks of life can now be imaged at sub-cellular resolution. A revolutionary technique is cryo-electron microscopy (cryo-EM), which is commonly used for single particle analysis of viruses, proteins, and other macromolecules [3]. In cryo-EM, samples are frozen at cryogenic temperatures and a series of 2-D projection images are taken at a variety of unknown angles with an electron microscope [3]. Reconstruction of the 3-D structure fundamentally becomes an inverse problem, where the key is to identify the angular orientation of the projections.

Reconstruction algorithms fall broadly into two categories: conventional and deep learning based. Conventional methods can be further divided into two sub-categories. In the first sub-category, if projection angles are known or accurately estimated, the central slice theorem gives rise to methods such as filtered back projection [4]. If orientation angles are unknown, reconstruction is posed as a non-convex optimization problem [5]. Evidently, reconstruction results are sensitive to initialisation and may converge to local minima over a large search space. On the other hand, learning-based methods have emerged as alternatives with the proliferation of GPU-based computing. One class of unsupervised networks (such as CryoGAN and CryoDRGN) does not require priors, but necessitates large training datasets for accurate performance [6], [7]. Other networks encode molecular information in reference based representation. In particular, AtomVAE and CryoFOLD represent imaging subjects as mixtures of Gaussians [8], [9]. In all these cases, reconstruction is made additionally challenging due to experimental conditions, such as microscopic imaging aberrations and low signal to noise ratio [10].

In this paper, we propose a reconstruction method that uses a limited number of projections taken at unknown angles that can accurately recover 3-D objects of arbitrary shape. The key to this approach is based on the representation of any object as a summation of point sources sampled by a kernel. Specifically, projection samples can be described as signals with finite rate of innovation (FRI), allowing for the retrieval of point sources with conventional methods such as matrix pencil. Following this, projection orientations and 3-D structure can be obtained through variations of the method outlined in [11].

II. Problem Formulation

A. Data Acquisition

We approximate a 3-D object of arbitrary shape with the function $g(\mathbf{r}) = g(x, y, z)$, which is composed of a mixture of K isotropic basis functions $\varphi(\mathbf{r})$ located at $\{\mathbf{v}_k\}_{k=1}^K$ in $\mathbb{R}^3$ space:

$$g(\mathbf{r}) = \sum_{k=1}^{K} a_k \varphi(\mathbf{r} - \mathbf{v}_k). \tag{1}$$

We also impose the condition that $\sum_{k=1}^K \mathbf{v}_k = \mathbf{0}$. For $J \geq 3$ projections of the object captured at distinct angles, the orientation of each projection plane is described by the direction vector $\mathbf{d}_j \in \mathbb{R}^3$ and limited to the rectangular viewing window Π_j. The 2-D projections, $\{I_j(x, y)\}_{j=1}^J$, are thus obtained through the application of the Radon transform to $g(\mathbf{r})$, as described in Equation (2):

$$\begin{aligned} I_j(\mathbf{x}) &= I_j(x, y) = \mathcal{P}_j\{g(\mathbf{r})\}(x, y) \\ &= \int_{\mathbb{R}^3} g(\mathbf{r})\delta(x - \mathbf{r}^T\mathbf{u}_{j,x} - s_{j,x})\delta(y - \mathbf{r}^T\mathbf{u}_{j,y} - s_{j,y})d^3\mathbf{r} \end{aligned} \tag{2}$$

This work was in part supported by BBSRC under Grant BB/Y513878/1.

where

- $\mathcal{P}_j\{\cdot\}$ denotes the projection operator onto the 2-D observation window Π_j.
- $\mathbf{u}_j = [\mathbf{u}_{j,x}, \mathbf{u}_{j,y}] \in \mathbb{R}^3$ are the unit vectors of the projection plane Π_j. Consequently, they obey the following relations: $\mathbf{u}_{j,x} \perp \mathbf{u}_{j,y}$ and $\mathbf{u}_{j,x} \times \mathbf{u}_{j,y} = \mathbf{d}_j, j = 1, ..., J$.
- $\mathbf{s}_j = [s_{j,x}, s_{j,y}] \in \mathbb{R}^2$ denotes the shifts of the projection plane along $\mathbf{u}_j$ in their respective x and y directions.

This process is illustrated in Figure 1.

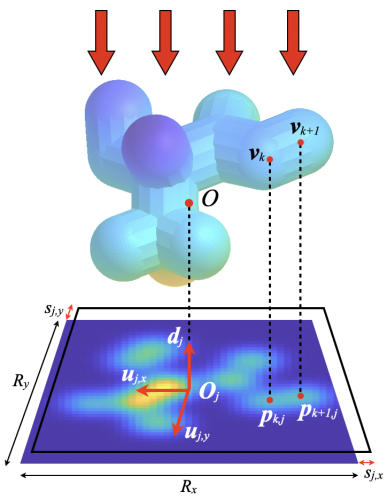

Fig. 1: An example of a 3-D shape $g(\mathbf{r})$ and its parallel beam projection onto Π_j. The origin of the projection is located at O_j at a shift $\mathbf{s}_j$ away from the true origin.

Considering the model description in Equation (1), the continuous 2-D projection can be described as follows,

$$\begin{aligned} I_j(\mathbf{x}) = I_j(x,y) &= \sum_{k=1}^{K} a_k \mathcal{P}_j\{\varphi(\mathbf{r}-\mathbf{v}_k)\} \\ &= \sum_{k=1}^{K} a_k \mathcal{P}_j\{\varphi\}(\mathbf{x}-\mathbf{p}_{k,j}) \end{aligned} \tag{3}$$

where $\mathbf{p}_{k,j} = [p^x_{k,j}, p^y_{k,j}] \in \mathbb{R}^2$ is the projection of the kth source $\mathbf{v}_k$ onto Π_j. Since $\varphi(\mathbf{r})$ is assumed to be isotropic and radially symmetric in 3-D, its 2-D projections $\mathcal{P}_j\{\varphi\}(\mathbf{x})$ are identical regardless of orientation. From Equation (2), the 2-D locations of the projected point sources $\mathbf{p}_{k,j}$ can be written in terms of their 3-D positions $\mathbf{v}_k$, unit vectors $\mathbf{u}_j$ and shifts $\mathbf{s}_j$ as follows:

$$\mathbf{p}_{k,j} = [\mathbf{v}_k^T \mathbf{u}_{j,x} + s_{j,x}, \mathbf{v}_k^T \mathbf{u}_{j,y} + s_{j,y}]^T. \tag{4}$$

The process of capturing a projection on a physical imaging sensor discretizes the image. The sampled discrete projection image $I_j[m,n]$ can then be modelled as follows:

$$\begin{aligned} I_j[m,n] &= \langle I_j(x,y), \delta(x/T_x - m, y/T_y - n)\rangle \\ &= \iint_{-\infty}^{\infty} I_j(x,y)\delta(x/T_x - m, y/T_y - n)dxdy \\ &= \sum_{k=1}^{K} a_k \mathcal{P}_j\{\varphi\}(mT_x - p^x_{k,j}, nT_y - p^y_{k,j}) \end{aligned} \tag{5}$$

where $\langle\cdot,\cdot\rangle$ denotes the inner product and T_x and T_y are the sampling periods along $\mathbf{u}_{j,x}$ and $\mathbf{u}_{j,y}$, respectively. Here, we assume for simplicity point-like sampling, but our approach can handle cases where filtering happens before sampling.

Since $g(\mathbf{r})$ is the summation of isotropic 3-D functions located at $\{\mathbf{v}_k\}$, the problem of reconstructing $g(\mathbf{r})$ is akin to recovering point sources and their amplitudes in $\mathbb{R}^3$ space.

B. Sampling Interpretation

The discrete signal $I_j[m,n]$ can be interpreted as the projection of a sum of 3-D Dirac delta functions, $\sum_{k=1}^{K} a_k \delta(\mathbf{r}-\mathbf{v}_k)$, onto the plane Π_j. This projection is subsequently filtered using a 2-D function $\mathcal{P}_j\{\varphi\}(\mathbf{x})$ and uniformly sampled along $\mathbf{u}_{j,x}$ and $\mathbf{u}_{j,y}$ with sampling periods T_x and T_y, respectively. Moreover, it belongs to the class of signals with finite rate of innovation due to its composition of isotropic 3-D functions [16]. As such, the acquisition process illustrated in Section II-A is equivalent to sampling the 2-D tomographic projection of a 3-D FRI signal at unknown angles.

In conventional sampling schemes, perfect reconstruction of classes of FRI signals is possible given appropriate selection of sampling kernel and reconstruction strategy. Of particular interest to our application is the class of exponential reproducing kernels [13]. In this paper, for the sake of problem stability and generalization, we loosen the exact reproduction requirement to that of exponential approximation, and make use of the generalized Kaiser-Bessel window function (KBWF) $\varphi(\mathbf{r})$, which has compact support and rotational symmetry [12]. As such, it is a commonly used basis function in tomography. The KBWF is given below in Equation (6), where w is the order of the modified Bessel function $\mathcal{I}_w(\cdot)$, $\gamma > 0$ is the window taper, and $b > 0$ is the support radius. Note that $\boldsymbol{\rho} \in \mathbb{R}^N, N \in \mathbb{Z}^+$ and $||\boldsymbol{\rho}||$ refers to the Euclidean norm.

$$\varphi(\boldsymbol{\rho}) = \begin{cases} \frac{\left(\sqrt{1-(||\boldsymbol{\rho}||/b)^2}\right)^w \mathcal{I}_w\left(\gamma\sqrt{1-(||\boldsymbol{\rho}||/b)^2}\right)}{\mathcal{I}_w(\gamma)} & 0 \le ||\boldsymbol{\rho}|| \le b, \\ 0 & \text{otherwise.} \end{cases} \tag{6}$$

The Radon transform of the KBWF admits a closed form expression as provided in [12]. In the context of FRI, unlike ideal sampling kernels (e.g., exponential splines) that allow for perfect reconstruction, the KBWF does not inherently guarantee exact recovery of the innovation parameters due to its approximate nature.

In the following section, we will demonstrate reconstruction of an arbitrarily shaped 3-D object (modeled with $g(\mathbf{r})$ in Equation (1) with $K \ge 4$) given $J \ge 3$ sampled projections. We start by recovering the projected vertices $\{\mathbf{p}_{k,j}\}$ and amplitudes $\{a_k\}$ from the discrete 2-D projections $I_j[m,n]$. Next, we perform parameter pairing across projections to simultaneously identify the vectors $\{\mathbf{u}_j\}$, $\{\mathbf{d}_j\}$, and $\{\mathbf{s}_j\}$, allowing for recovery of the 3-D object.

III. Reconstruction Method

A. Recovering $\mathbf{p}_{k,j}$ and a_k

The first step in reconstruction is recovering the 2-D parameters $\{\mathbf{p}_{k,j}\}$ and $\{a_k\}$ in each projection. Since the

KBWF cannot exactly reproduce exponentials, we leverage the approximate reproduction framework proposed in [13]. We start by finding the coefficients $c^{\alpha,\beta}_{(r,q),(m,n)}$ in the following approximation, where $\alpha_r = \alpha_0 + r\zeta, r = 0, 1, ..., R$ and $\beta_q = \beta_0 + q\xi, q = 0, 1, ..., Q$:

$$\sum_{m,n\in\mathbb{Z}} c^{\alpha,\beta}_{(r,q),(m,n)} \mathcal{P}_j\{\varphi\}\left(x/T_x - m, y/T_y - n\right) \approx e^{\alpha_r x} e^{\beta_q y}. \tag{7}$$

The coefficients are calculated using the interpolation formula in [13], which allows the reproduced function from the *lhs* of Equation (7) to interpolate the exponentials at each integer point. The 2-D generalization of the interpolation formula is provided below:

$$c^{\alpha,\beta}_{(r,q),(m,n)} = \frac{1}{\sum_{h,l\in\mathbb{Z}} e^{-\alpha_r h} e^{-\beta_q l} \mathcal{P}_j\{\varphi\}(h,l)} e^{\alpha_r m} e^{\beta_q n}. \tag{8}$$

The coefficients are then used to calculate the exponential moments, τ_{rq}, of the projection signal. Specifically:

$$\begin{aligned}
\tau_{rq} &= \sum_{m,n} c^{\alpha,\beta}_{(r,q),(m,n)} I_j[m,n] \\
&\overset{(a)}{=} \langle I_j(x,y), \sum_{m,n} c^{\alpha,\beta}_{(r,q),(m,n)} \mathcal{P}_j\{\varphi\}(x/T_x - m, y/T_y - n)\rangle \\
&\overset{(b)}{\approx} \langle \sum_{k=1}^{K} a_k \delta(\mathbf{x} - \mathbf{p}_{k,j}), e^{\alpha_r x} e^{\beta_q y}\rangle \\
&\overset{(c)}{=} \int_{-\infty}^{\infty} \sum_{k=1}^{K} a_k \delta(\mathbf{x} - \mathbf{p}_{k,j}) e^{\alpha_r x} e^{\beta_q y} dxdy \\
&= \sum_{j,k} a_k e^{\alpha_r p^x_{k,j}} e^{\beta_q p^y_{k,j}} = \sum_{j,k} \hat{a}_{k,j} \mu_k^r \lambda_k^q
\end{aligned} \tag{9}$$

where (a) is from the linearity of the inner product, (b) follows from Equation (7), and (c) represents the rth and q^{th} approximate exponential moment of $I_j(x,y)$. The exponential moments can be expressed as the form in the final line of Equation (9), where $\hat{a}_{k,j} = a_k e^{\alpha_0 p^x_{k,j}} e^{\beta_0 p^y_{k,j}}$ and $\mu_k = e^{\zeta p^x_{k,j}}, \lambda_k = e^{\xi p^y_{k,j}}$. The choice of R and Q in α_r and β_q determines the number of moments, where $R, Q \geq 2K - 1$.

The amplitudes $\hat{a}_{k,j}$ and locations μ_k, λ_k can be found through a variety of 2-D harmonic retrieval techniques. In our case, we make use of the algebraically coupled matrix pencil (ACMP) algorithm presented in [14] for simultaneous and accurate retrieval of μ_k and λ_k.

The next step is finding the amplitudes of the exponential moments, which becomes the simple task of solving a Vandermonde system with an unique solution. The final step in identifying projection parameters is to account for geometric shifts, which is solved for using the following expression given for the x direction:

$$\sum_{k=1}^{K} p^x_{k,j} \overset{(d)}{=} \left(\sum_{k=1}^{K} \mathbf{v}_k^T\right) \mathbf{u}_{j,x} + K s_{j,x} \overset{(e)}{=} K s_{j,x} \tag{10}$$

where (d) is based on Equation (4) and (e) follows from the fact that the geometric center of $\{\mathbf{v}_k\}$ is at the origin. The same expression is applied to determine the shift in the y direction.

B. Pairing Across Projections

Given the positions and amplitudes of the projected 2-D functions for each $I_j[m,n]$, the next task is to pair them across the different projections. Namely, we want to determine if $\mathbf{p}_{k,j}$ and $\mathbf{p}_{k',l}$ in $I_j[m,n]$ and $I_l[m,n]$ correspond to the same point $\mathbf{v}_k$ in 3-D. This pairing is done through amplitude comparison and rank criterion, with the latter outlined in [11].

We first use the recovered amplitude information as an initial pass for pairing across different projections. If two recovered amplitudes $a_{k,j}$ and $a_{k',l}$ from different projections can be uniquely associated, then their corresponding 2-D location $\mathbf{p}_{k,j}$ and $\mathbf{p}_{k',j}$ are inferred to correspond to the same 3-D point $\mathbf{v}_k$. Therefore, we start by pairing all sets of $\mathbf{p}_{k,j}$ and $\mathbf{p}_{k',l}$ with unique and identical amplitudes. We take the paired 2-D locations and arrange them into the matrix Υ_1:

$$\Upsilon_1 = \begin{bmatrix} \mathbf{p}^T_{1,j} & \mathbf{p}^T_{1,l} \\ \mathbf{p}^T_{2,j} & \mathbf{p}^T_{2,l} \\ \vdots & \vdots \\ \mathbf{p}^T_{L,j} & \mathbf{p}^T_{L,l} \end{bmatrix}, \tag{11}$$

where the rows consist of correctly paired projection points. In [11], it is shown that correctly paired projection points yields a rank deficient matrix Υ, with maximum rank 3, so we use this condition to validate our pairing.

Assuming that L pairs have been matched, the subset of remaining $(K - L)$ parameters are used to create the matrix Υ_2. Following the method in [11], the order of rows in one column are permuted until rank deficiency is achieved. The initial step of pairing with amplitudes reduces the number of permutations required from $K!$ to $(K-L)!$, which significantly eases computation time. When the correct pairing is reached, all K values of $\mathbf{p}_{k,j}$ and $\mathbf{p}_{k',l}$ form a rank deficient matrix Υ:

$$\Upsilon = \begin{bmatrix} \Upsilon_1 \\ \Upsilon_2 \end{bmatrix} = \begin{bmatrix} \mathbf{p}^T_{1,j} & \mathbf{p}^T_{1,l} \\ \mathbf{p}^T_{2,j} & \mathbf{p}^T_{2,l} \\ \vdots & \vdots \\ \mathbf{p}^T_{K,j} & \mathbf{p}^T_{K,l} \end{bmatrix}. \tag{12}$$

This is used to determine the unit vectors $\mathbf{u}_j$ and by extension, the projection angles.

C. Projection Angle Estimation

The steps for estimating projection orientations follows the procedure outlined in [11]. We start by creating $\mathbf{\Omega}_x$ from the paired projection positions, which is defined below. Note that $\mathbf{\Omega}_y$ is created in a similar manner.

$$\mathbf{\Omega}_x = \begin{bmatrix} \mathbf{p}^x_{1,1} \cdots \mathbf{p}^x_{1,J} \\ \vdots \\ \mathbf{p}^x_{1,K} \cdots \mathbf{p}^x_{K,J} \end{bmatrix}_{K\times J} = \begin{bmatrix} \mathbf{v}_1^T \\ \vdots \\ \mathbf{v}_K^T \end{bmatrix}_{K\times 3} \begin{bmatrix} \mathbf{u}_{1x} & \cdots & \mathbf{u}_{Jx} \end{bmatrix}_{3\times J} = \mathbf{V}\mathbf{U}_x \tag{13}$$

$\mathbf{\Omega}_x$ and $\mathbf{\Omega}_y$ are concatenated to form $\mathbf{\Omega} = [\mathbf{\Omega}_x|\mathbf{\Omega}_y]$. Evidently, $\mathbf{\Omega}$ can be factorized as $\mathbf{\Omega} = \mathbf{V}[\mathbf{U}_x|\mathbf{U}_y] = \mathbf{V}\mathbf{U}$. Next, the singular value decomposition of $\mathbf{\Omega} = \mathcal{U}\mathcal{S}\mathcal{V}^T$ yields the first estimate for $\mathbf{U}$, denoted as $\hat{\mathbf{U}}$:

$$\hat{\mathbf{U}} = [\hat{\mathbf{U}}_x|\hat{\mathbf{U}}_y] = \mathcal{S}\mathcal{V}^T. \tag{14}$$

This initial estimate is related to the true unit vectors through the linear transform $\mathbf{Q} \in \mathbb{R}^{3\times 3}$, where $\mathbf{U} = \mathbf{Q}\hat{\mathbf{U}}$. Using the fact that $\mathbf{U}$ has unit norm columns, we can state the following relations: $\hat{\mathbf{u}}_{j,x}^T\mathbf{Q}^T\mathbf{Q}\hat{\mathbf{u}}_{j,x} = 1$ and $\hat{\mathbf{u}}_{j,y}^T\mathbf{Q}^T\mathbf{Q}\hat{\mathbf{u}}_{j,y} = 1$, which yield a system of $2J$ linear equations altogether. Defining $\mathbf{M} = \mathbf{Q}^T\mathbf{Q}$, we recognize that it is a symmetric matrix with six unknowns, thus requiring at least six (=$2J$) equations to solve, necessitating the condition $J \geq 3$. This is solved to identify $\mathbf{Q}$, which is then applied to $\mathbf{U}$ to obtain the true unit vectors of each projection. Finally, the direction vectors $\mathbf{d}_j$ are computed using cross product between the $\mathbf{u}_{j,x}$ and $\mathbf{u}_{j,y}$, up to a rigid rotation.

D. 3-D Object Recovery

Once the unit direction vectors are found, $\mathbf{v}_k$ is determined from the series of linear equations formed by $\mathbf{\Omega}_x$ and $\mathbf{\Omega}_y$. Using the 3-D geometric centers and amplitudes, the 3-D object is fully reconstructed using Equation (1).

Therefore, given $I_j[m,n], j = 1,...,J$ with $J \geq 3$ at unknown orientations, the projection angles and the arbitrary 3-D object comprised of $K \geq 4$ isotropic functions can be exactly reconstructed up to an orthogonal transformation. The full method is summarized in Algorithm 1.

Algorithm 1 Full 3-D shape reconstruction algorithm

Inputs: 2-D projections $\{I_j[m,n]\}_{j=1}^J$, $J \geq 3$
Outputs: 3-D geometric centers $\{\mathbf{v}_k\}_{k=1}^K$, projection orientations $\{\mathbf{d}_k\}_{k=1}^K$, 2-D planar shifts $\{s_j\}_{j=1}^J$, $K \geq 4$

1: Compute the exponential moments τ_{rq} for each projection based on Equation (9).
2: Apply 2-D harmonic retrieval to the exponential moments to recover amplitudes a_k and positions $\mathbf{p}_{k,j}$.
3: Calculate 2-D planar shifts by solving Equation (10) and apply corrections to $\mathbf{p}_{k,j}$.
4: Pair sets of $\{\mathbf{p}_{k,j}\}_{k=1}^L, L \leq K$ based on amplitudes a_k.
5: Pair the remaining sets of $(K-L)$ points $\{\mathbf{p}_{k,j}\}_{k=L+1}^K$ based on the rank criterion.
6: Determine the unit direction vectors $\mathbf{u}_{j,x}, \mathbf{u}_{j,y}$ of each projection by applying SVD to $\mathbf{\Omega}$ and then finding $\mathbf{Q}$.
7: Compute the orientations of each projection $\mathbf{d}_j$ by taking the cross product between $\mathbf{u}_{j,x}$ and $\mathbf{u}_{j,y}$.
8: Find the geometric centers $\{\mathbf{v}_k\}_{k=1}^K$ from the series of linear equations formed by $\mathbf{\Omega}_x$ and $\mathbf{\Omega}_y$
9: Reconstruct the full 3-D object using Equation (1).

IV. Numerical Simulation

The method outlined above is applied to $g(\mathbf{r})$ comprised of $K = 12$ isotropic functions and $J = 3$ projections at randomly selected orientations. In the spirit of cryo-EM based applications, we select the molecular model of polylactic acid (PLA) as positional reference for $g(\mathbf{r})$ [17]. The 3-D model and its 3 random projections are shown in Figure 2. The

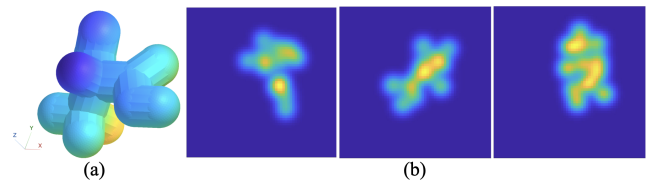

Fig. 2: $g(\mathbf{r})$ comprised of 12 isotropic functions. (a) shows the 3-D molecular model and (b) shows projections of (a) at 3 random orientations.

isotropic function is the 2-D KBWF with modified Bessel order $w = 2$, support radius $b = 0.1$, and window taper $\gamma = 19$. Exponential approximation coefficients are calculated using the interpolation formula provided in Equation (8). The sampling period is $T_x = T_y = 1/62$. The first step of reconstruction is applying the method outlined in Section III to accurately determine the geometric centers $\mathbf{p}_{k,j}$ and amplitudes $a_{j,k}$ of the molecules, which are demonstrated for a selected projection in Figure 3. Finally, the recovered object along with its unit vectors are shown in Figure 4.

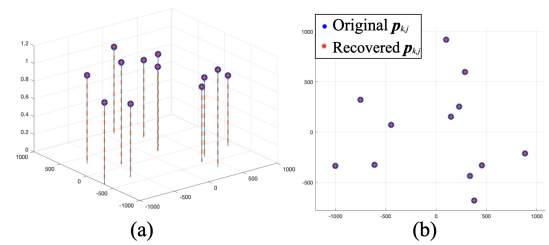

Fig. 3: The original and recovered 2-D FRI parameters. (a) shows accurate a_k values at locations $\mathbf{p}_{k,j}$ and (b) shows $\mathbf{p}_{k,j}$ directly for a projection.

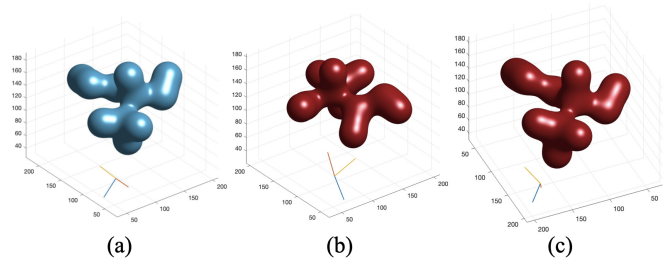

Fig. 4: The original and reconstructed object with $\mathbf{u}_j$ and $\mathbf{d}_k$. (a) shows $g(\mathbf{r})$, (b) shows the recovered object, and (c) shows the recovered object after applying an orthogonal transformation.

V. Conclusion

We have proposed a method for accurate reconstruction of an arbitrarily shaped 3-D object from $J \geq 3$ 2-D projections while simultaneously identifying unknown projection orientations. In the future, we will analyse resiliency of the method to noise and we will study how to increase noise resiliency with the number J of projections.

REFERENCES

[1] G. T. Papadopoulos and P. Daras, "Human action recognition using 3D reconstruction data," *IEEE Transactions on Circuits and Systems for Video Technology*, vol. 28, no. 8, pp. 1807-1823, 2018

[2] U. Khan, A. Yasin, M. Abid, I. Shafi, and S. A. Khan, "A methodological review of 3D reconstruction techniques in tomographic imaging," *Journal of Medical Systems*, vol. 42, no. 190, 2018.

[3] J. L. Milne, M. J. Borgnia, A. Bartesaghi, E. E. Tran, L. A. Earl, D. M. Schauder, J. Lengyel, J.Pierson, A. Patwardhan, and S. Subramaniam, "Cryo-electron microscopy: a primer for the non-microscopist," *The FEBS Journal*, vol. 280, pp. 28-45, 2012.

[4] G. N. Hounsfield, "Computerized transverse axial scanning (tomography): part 1. description of system," *British Journal of Radiology*, vol. 46, no. 552, pp. 1016–1022, 1973.

[5] C. Donnat, A. Levy, F. Poitevin, E. D. Zhong, and N. Miolane, "Deep generative modeling for volume reconstruction in cryo-electron microscopy," *Journal of Structural Biology*, vol. 214, no. 4, 2022.

[6] H. Gupta, M. T. McCann, L. Donati and M. Unser, "CryoGAN: a new reconstruction paradigm for single-particle cryo-EM via deep adversarial learning," *IEEE Transactions on Computational Imaging*, vol. 7, pp. 759-774, 2021.

[7] E. D. Zhong, T. Bepler, B. Berger, and J. H. Davis, "CryoDRGN: reconstruction of heterogeneous cryo-EM structures using neural networks," *Nature Methods*, vol. 18, pp. 176–185, 2021.

[8] D. Rosenbaum, M. Garnelo, M. Zielinski, C. Beattie, E. Clancy, A. Huber, P. Kohli, A. W. Senior, J. Jumper, C. Doersch, S. M. A. Eslami, O. Ronneberger, and J. Adler, "Inferring a Continuous Distribution of Atom Coordinates from Cryo-EM Images using VAEs," arXiv:2106.14108 [cs.CE], 2021.

[9] E. D. Zhong, A. Lerer, J. H. Davis, B. Berger, "Exploring generative atomic models in cryo-EM reconstruction," arXiv:2107.01331 [q-bio.BM], 2021.

[10] A. Chari and H. Stark, "Prospects and limitations of high-resolution single-particle cryo-electron microscopy," *Annual Review of Biophysics*, vol. 52, pp. 391-411, 2023.

[11] R. Wang, F. G. Bossema, T. Blu, P. L. Dragotti, "Reconstructing classes of 3D FRI signals from sampled tomographic projections at unknown angles," arXiv:2404.09969 [eess.SP], 2024.

[12] M. Nilchian, J. P. Ward, C. Vonesch, and M. Unser, "Optimized Kaiser-Bessel window functions for computed tomography," *IEEE Transactions on Image Processing*, vol. 24, no. 11, 2015.

[13] J. A. Urigüen, T. Blu, and P. L. Dragotti, "FRI sampling with arbitrary kernels," *IEEE Transactions on Signal Processing*, vol. 61, no. 21, pp. 5310-5323, 2013.

[14] F. Vanpoucke, M. Moonen, Y. Berthoumieu, "An efficient subspace algorithm for 2-D harmonic retrieval," *Proc. IEEE Int. Conf. Acoust., Speech Signal Process*, 1994, pp. 461-464.

[15] R. Wang and P. L. Dragotti, "Perfect reconstruction of classes of 3D non-bandlimited signals from gomographic projections at unknown angles," *2023 31st European Signal Processing Conference (EUSIPCO)*, 2023, pp. 1903-1907.

[16] P. L. Dragotti, M. Vetterli and T. Blu, "Sampling Moments and Reconstructing Signals of Finite Rate of Innovation: Shannon Meets Strang–Fix," in *IEEE Transactions on Signal Processing*, vol. 55, no. 5, pp. 1741-1757, May 2007.

[17] National Institutes of Health, "PLA," 3d.nih.gov. https://3d.nih.gov/entries/3DPX-014616 (accessed Jan 2025).